J. Fluid Mech. (1988), *vol.* 189, *pp.* 531–552
Printed in Great Britain

The structure of turbulent shear-induced countercurrent flow

By IOANNIS K. TSANIS
National Water Research Institute, Canada Centre for Inland Waters, Burlington, Ontario, L7R 4A6, Canada

AND HANS J. LEUTHEUSSER
Department of Mechanical Engineering, University of Toronto, Toronto, Ontario, M5S 1A4, Canada

(Received 6 August 1986 and in revised form 2 October 1987)

Countercurrent flow is a generalized plane Couette flow in which a shear-induced drift current is opposed by a pressure-driven return flow such that the resulting mass flux is zero. This type of flow is encountered in both environmental fluid mechanics and tribology. Measurements are described that were undertaken in steady turbulent countercurrent flow, generated in a novel type of apparatus between smooth walls, at Reynolds numbers, expressed in terms of surface velocity and depth of the flow, from 200 to 20000; the critical Reynolds number of laminar to turbulent transition as determined herein is approximately 1750. The laboratory facility is explained, and experimental data are presented on mean velocities, pressure gradient, turbulence intensities, Reynolds stresses, and energy spectra. It is found that the velocity distributions follow the universal law of the wall in the drift current, but that the flow is undeveloped in the return portion of the flow. The non-dimensional longitudinal pressure gradient increases with Reynolds number, and a semi-empirical law of resistance is proposed and experimentally verified. Turbulence intensities in the drift current increase toward the shearing surface but are essentially constant in the opposing pressure-driven flow. The distribution of the Reynolds stress is found to be consistent with previous measurements obtained in this type of flow using different apparatus, but only approximately follows the theoretically linear distribution. Energy spectra in the shear-induced portion of the flow involve higher frequencies closer to the shearing surface than in the return current. There, the spectral energy is essentially the same throughout the flow, reflecting the constancy of turbulent intensity in this region.

1. Introduction

Besides generating surface waves, the wind acting on a quiescent body of water produces a shear-induced drift current and accompanying slight upward tilt, or wind set-up, of the water surface in a downwind direction, and a mass-balancing gravity-driven return current near the bottom. The resulting two-layer shear flow, often rendered complicated by Coriolis effects due to the Earth's rotation and density stratification of the water body, represents the primary mechanism for the dispersion and diffusion of contaminants in lakes and small ocean bays.

Notwithstanding its environmental importance, however, the present understanding of this flow is still rather limited, being based on a relatively small number

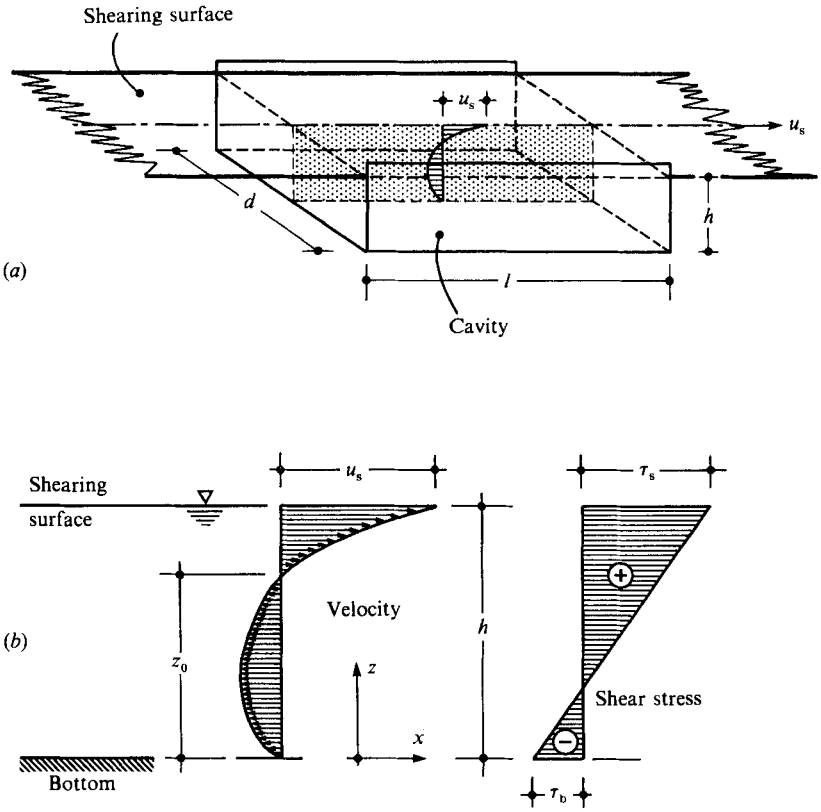

FIGURE 1. Definitions diagrams: (*a*) laboratory system; (*b*) flow parameters.

of often inconclusive laboratory studies undertaken in combined wind and water, or air–sea interaction, tunnels. Results obtained in these experimental systems by Forssbland (1974), Tichner (1958), Masch (1963), Baines & Knapp (1965), Goossens (1979), Koutitas & O'Connor (1980) and Goossens, van Pagee & Tessel (1982) have been found to be highly three-dimensional on both the air side and the water side of the interface due to sidewall friction effects. Among other consequences, this leads to velocity distributions in the centreplane, i.e. the principal measuring plane, of the induced water flow that have non-zero net volume flux. Furthermore, because of the finite longitudinal extent of laboratory facilities, surface wave patterns are produced that do not correspond to prototype conditions.

Recognizing both the limitations of the available experimental data and the shortcomings of the conventional modelling systems, an entirely new approach towards the physical simulation of wind-induced currents is pursued in the present work. In this, the body of water subject to wind action is simulated by a volume of air contained inside a cavity, and shear is applied directly to the fluid by sliding the cavity past a stationary plane surface representing the air–water interface, see figure 1 (*a*). The result is a 'driven cavity' of the kind frequently used by numerical analysts as a test case in computational fluid mechanics; see e.g. Gatski, Grosh & Rose (1982) and Gustafson & Halasi (1986). In the physical realization of interest herein, the flow in the cavity is essentially homogeneous, two-dimensional and parallel, and comprises a shear-induced current adjacent to the exposed, or shearing surface of the cavity, and an opposing pressure-driven current near its bottom; figure 1 (*b*) is a definition

diagram of this flow. The fluid motion may be descriptively referred to as shear-induced countercurrent flow and, obviously, corresponds to a general case of plane Couette flow. As such, it is encountered not only in the form of idealized wind-driven water currents, but also in the guise of thin fluid films occurring in hydrodynamic bearings.

The new modelling approach sketched in the foregoing overcomes some of the problems plaguing the conventional laboratory systems. Thus, the velocity distribution in the transverse direction is essentially uniform because of minimized sidewall effects and, as a result, continuity in streamwise planes is essentially preserved; the roughness, i.e. the waviness, of the free surface can be controlled; and, last but not least, the experimentally simple hot-wire velocimetry technique can be used for turbulent quantity measurements because the working fluid is air. The present system is clearly superior not only to the conventional wind–water tunnels, but also to the belt-type apparatus first used by Reichardt (1956) in his pioneering studies of plane Couette flow, and employed by Huey & Williamson (1974), El Telbany & Reynolds (1981), and others in experimental investigation of plane channel flows. Unfortunately, it is the nature of moving belts to deform at high wall velocities. This not only disturbs the geometry of the system, but also prevents measurements from being taken close to the moving wall.

The present study is limited to turbulent countercurrent flow under hydrodynamically smooth wall conditions. This restriction is particularly acceptable within the context of environmental fluid mechanics since there are indications that the aqueous boundary layer of the air–water interface in the field functions generally in this regime (Wu 1973).

2. Equipment and experimental procedure

2.1. *Experimental facility*

An existing laboratory installation, originally constructed for the study of plane Couette flow of air (Aydin & Leutheusser 1979), was modified to suit the needs of the present experiment (Tsanis 1986). In the basic apparatus, one wall is propelled by the carriage of a towing-tank installation, and the other wall is the surface of a stationary bench which is constructed alongside the towing channel proper. The velocity of the propelling carriage can be varied continuously from zero up to a maximum of about 3 m/s, and the maximum acceleration is 0.80 m/s^2.

In order to produce countercurrent flow, the moving wall is enclosed on all four sides by Plexiglas plates, thus forming a box, or cavity. In the test rig the moving box is actually mounted above the stationary bench surface which acts as the shearing surface. However, both figure 1 and the contents of this paper are arranged to correspond to the physical situation of wind-generated water currents where shear is applied to the free surface, and the coordinate z is measured upwards from the bottom of the water body. The length l of the moving box is 2.40 m, and the width d is 0.72 m. The box straddles with its longitudinal side walls the 0.71 m wide stationary wall, and its depth h can be adjusted between a minimum of 0.01 m and a maximum of 0.15 m. Clearances between box and bench are closed by sliding seals.

The stationary wall is composed of panels of plate glass situated on top of a 31 m long aluminium bench. The top surface of the glass panels is coplanar with the horizontal plane of the carriage track. The glass-covered bench begins and terminates 14.5 m away from the two end points of the 60 m long towing channel. The required

distances for accelerating and decelerating the carriage to and from its maximum velocity are less than 14.5 m. Based on this, the whole length of the stationary bench is available for testing purposes under steady-state conditions over the whole range of carriage velocities.

A shortcoming of the present apparatus is the finite time available for measurement purposes. Thus, at the maximum carriage velocity of 3 m/s, the minimum duration of a 31 m long run at constant speed is slightly more than 10 s. This short time may necessitate a large number of repetitious tests in order to evaluate completely the distribution of a particular flow property.

2.2. *Incidental measuring devices*

The velocity and the position of the towing carriage are determined electronically. To this end, optical switches are located 1 m, 18 m and 28 m downstream from the leading end of the stationary bench. Each switch, when interrupting the light ray emitted by the sensor, sends a pulse to a recorder. The first optical switch starts a stopwatch, and the remaining two, which are precisely 10 m apart, are used to determine the speed of the carriage. The resulting mean carriage velocity over the base distance is estimated to be accurate to within 0.01 m/s.

The position of the carriage is established with the aid of a position counter in conjunction with 63 stainless-steel strips equally spaced along the length of the stationary bench. The strips function as reflectors and activate the counter by means of a light sensor. The position counter is also connected with a pulse generator used for flow visualization by the smoke-wire technique. As soon as the external switch of the pulse generator is activated, the position counter stops and remains in the locked position while at the same instance a still camera is fired. This documents the position in which the picture is taken. A reset switch resumes the operation of the position counter.

2.3. *Hot-wire velocimetry*

Properties of the induced flow inside the moving box are determined with standard hot-wire velocimetry equipment which is stored aboard the towing carriage. Single-wire probes are used to measure mean velocities, turbulence intensities and frequency spectra in the flow-, or x-direction, while X-wire probes are employed for the measurement of Reynolds stress, and intensities in the x- and z-directions.

The hot-wire sensors can be moved both vertically, by means of a sweep-drive unit driven by an external stepper motor, and horizontally by means of a constant-velocity traversing mechanism. Controlled horizontal movement is required to provide a d.c.-component to the turbulent signal in the region of flow reversal.

Calibration of the hot-wire sensors is effected with the experimental apparatus itself. In particular, for velocities greater than 0.2 m/s, the probe to be calibrated is fixed to the carriage and towed inside a protective sheath affixed to the stationary bench (Aydin & Leutheusser 1980). For velocities smaller than 0.2 m/s, the probe is moved horizontally inside the box, with the latter at rest, and the speed of the sensor is determined by timing its movement over a distance of 0.70 m using optical switches (Tsanis 1987).

2.4. *Data acquisition*

During the tests voltages from the hot-wire bridges are monitored continuously with digital and r.m.s. voltmeters. An integrating constant of 3 s provides stable readings of mean and r.m.s. voltages even during the shortest runs. Each measurement point is repeated several times to obtain a reliable average reading.

In addition, the electronic signals from the hot-wire sensors are recorded on magnetic tape. The peak voltage of the recording is scaled down in order to include all instantaneous fluctuations between ± 1 V. A large signal-to-noise ratio is obtained by running the recording tape at a speed of 38 cm/s. In each test the recorder is started at the instant when the carriage is approximately 7 m away from the leading end of the stationary bench, and is kept running until the box has cleared the bench completely. The useful portion of the hot-wire signal is located in the data window defined by step signals originating from the 18 m and 28 m stations, i.e. the final 10 m of box travel over the stationary wall. In the case of laminar motion, the maximum length of travel required for the flow in a long cavity to become established, or 'spun up', is about 120 box depths (Tsanis & Leutheusser 1987); i.e. 15 m if $h = 0.12$ m. For turbulent flow the required length for flow spin-up is shorter. Hence, there is reason to believe that the cavity flow is always essentially established beyond the 18 m station.

Before being sent to the analog recorder the hot-wire signals are conditioned by applying a zero offset of 2.8 to 3.0 V, an amplification factor of 10, and low-pass filtering at 2 kHz. The low velocities used in the present investigation lead to an anticipated upper frequency limit of 2 kHz. In order to avoid aliasing, sampling is undertaken at a frequency of 4 kHz (Bendat & Piersol 1971).

To facilitate subsequent data evaluation, the analog signals are digitized using a 12 bit A/D converter. For carriage velocities between 1.5 m/s and 2.5 m/s, the duration of the signal for each run is between 4.00 and 6.66 s, and the resulting number of points are between 16000 and 25000, respectively. Since at least three runs are undertaken for each point, approximately 20 s of signal are available for computer processing, almost exactly the time required for an ensemble average to 3% accuracy (Lumley & Panofsky 1964). This suggests that the number of repeated runs used is sufficient to assure convergence of the turbulence quantities. The difference in the values of turbulence quantities between individual runs was found to be less than 10%. The same holds true for the differences between mean and r.m.s. velocities determined by voltmeters, and their digital counterparts. In the final evaluation of the digitized data, mean and r.m.s. values of the instantaneous velocities, turbulence intensities and Reynolds stresses are determined according to Vagt (1979). A fast-Fourier-transform algorithm is employed to evaluate the autospectrum. The 'hanning' weighting function is used as a window function in order to achieve a smooth estimate of the autospectrum by minimizing the leakage problem (Bendat & Piersol 1971).

2.5. *Flow visualization*

The principle of the smoke-wire technique (Goldstein 1983) is exploited to obtain an integrated view of the flow field in the centreplane of the moving box, and to locate the position of the zero-velocity point in the region of flow reversal. To this end, a nickel–chrome wire with diameter of 0.08 mm is held taut, in a vertical position in the centre of the box. The wire is coated with kerosene and, heated by the passage of an electric current pulse, produces a dense white smoke. Observations are recorded by both still photography and video cinematography. Two representative streakline pictures for, respectively, laminar flow ($R_s = 1300$) and turbulent flow ($R_s = 5000$) are reproduced in figure 2.

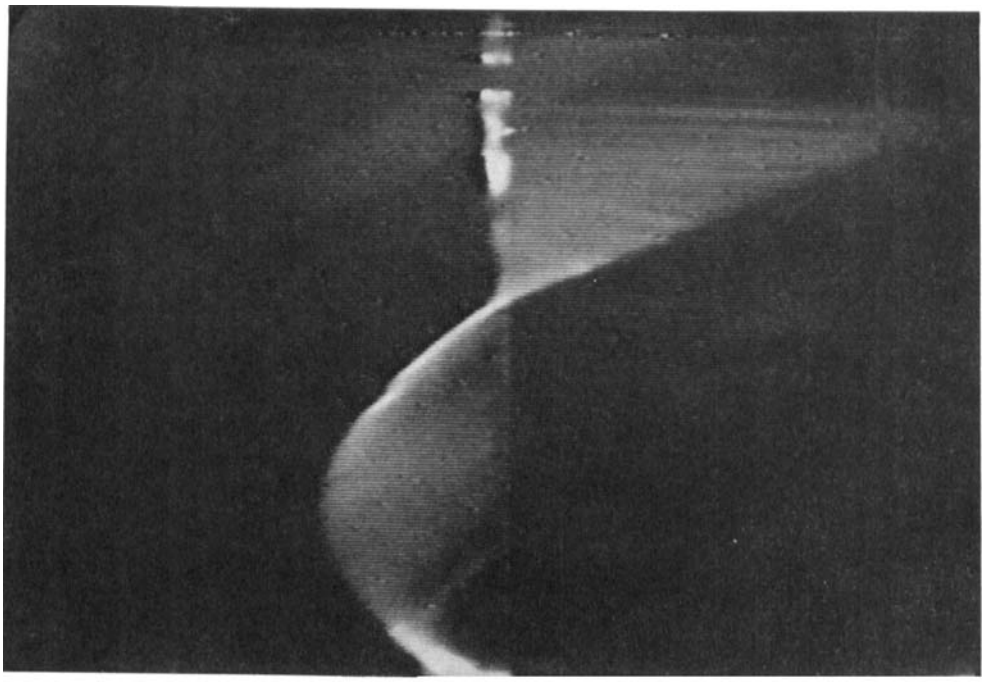

(a)

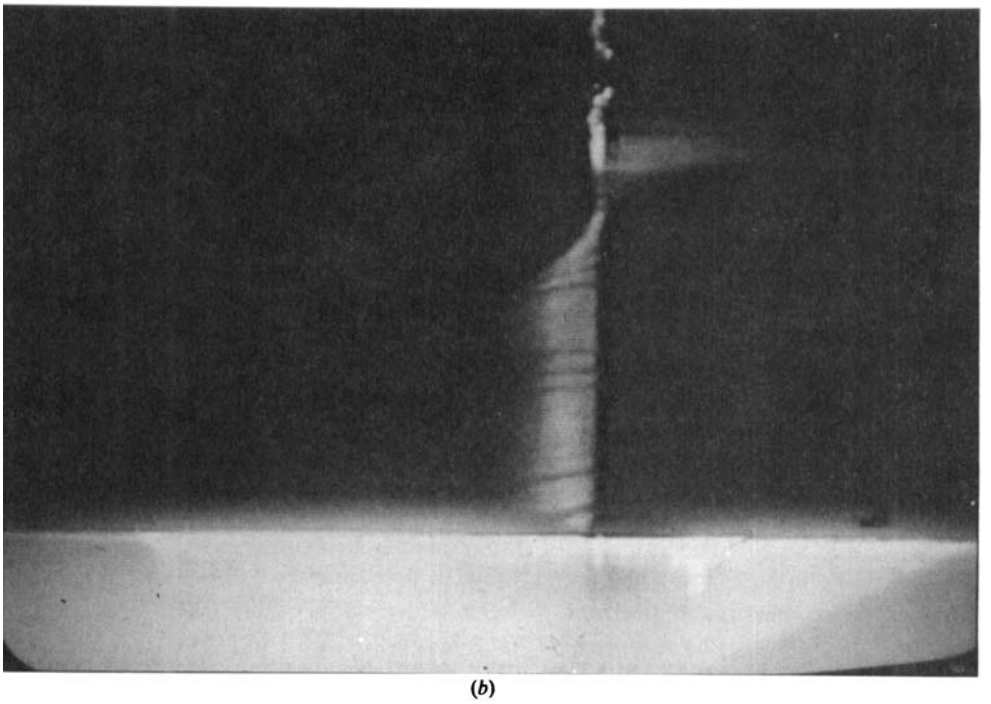

(b)

FIGURE 2. Video images of smoke-wire streaklines: (a) laminar flow ($R_s = 1300$); (b) turbulent flow ($R_s = 5000$).

3. Results and discussion

3.1. *Critical Reynolds number*

The transition from laminar to turbulent flow commences at some value of the Reynolds number below which even strong disturbances do not cause the flow to become unstable. The definition of this Reynolds number, and its lower critical value, vary between flows. For the countercurrent flow at hand the appropriate Reynolds number is

$$R_s = \frac{u_s h}{\nu}, \tag{1}$$

where u_s is the velocity of the shearing surface, h is the depth of flow, and $\nu = \mu/\rho$ is the kinematic viscosity; μ is the dynamic viscosity, and ρ is the density of the fluid.

In the present instance the critical Reynolds number was determined by observing the oscilloscope display of a hot-wire signal originating close to the shearing wall, i.e. at $z/h = 0.93$, in a flow with $h = 0.05$ m. To this end the velocity u_s was successively decreased in a series of tests until there was no more intermittency exhibited by the oscilloscope trace. The critical Reynolds number was thus found to be $(R_s)_{cr} = 1750 \pm 150$ which is in excellent agreement with Keulegan's (1951) observations of wind-induced water currents in an air–water interaction tunnel. This finding compares with $(R_s)_{cr} \approx 1200$ for plane Couette flow (Leutheusser & Chu 1971) and identifies countercurrent flow as the clearly more stable one (i.e. it is less susceptible to the development of an inflexion point in the laminar velocity profile) of these two related fluid motions.

3.2. *Distribution of mean velocity*

Measurements of velocity and related properties were effected by hot-wire velocimetry with the probe station located at the geometric centre of the box plane. In particular, a total of seven velocity traverses were performed at Reynolds numbers R_s between 2000 and 20000; four with a depth of flow $h = 0.05$ m, and three with $h = 0.12$ m. The uniformity and two-dimensionality of flow inside the moving box was verified by control measurements executed both upstream and downstream, and from the side of the box centre. Similarly, flow continuity was checked by separately calculating the volume fluxes per unit width of the drift and return currents. For $h = 0.05$ m, the drift portion was found to be over 90%, and for $h = 0.12$ m, over 80% of the return portion of the flow. This discrepancy is probably due to a combination of unavoidable air leakage from the moving box, and deteriorating flow parallelity with increasing depth. It is significantly smaller than that observed in conventional air–water systems where the volume flux per unit width of the drift current is generally less than 70% of the flux of the return current.

Typical distributions of the local streamwise mean velocity u for six Reynolds numbers and two depths of flow are depicted in figure 3. The simple non-dimensional data presentation of u/u_s *vs.* z/h is, of course, not universal under conditions of turbulent flow, and the profiles clearly become more uniform with increasing Reynolds number. However, there is no effect that could be attributed to changes in cavity geometry, and this supports the contention that fully developed flow prevails.

Also included in figure 3 is the parabolic velocity distribution for laminar

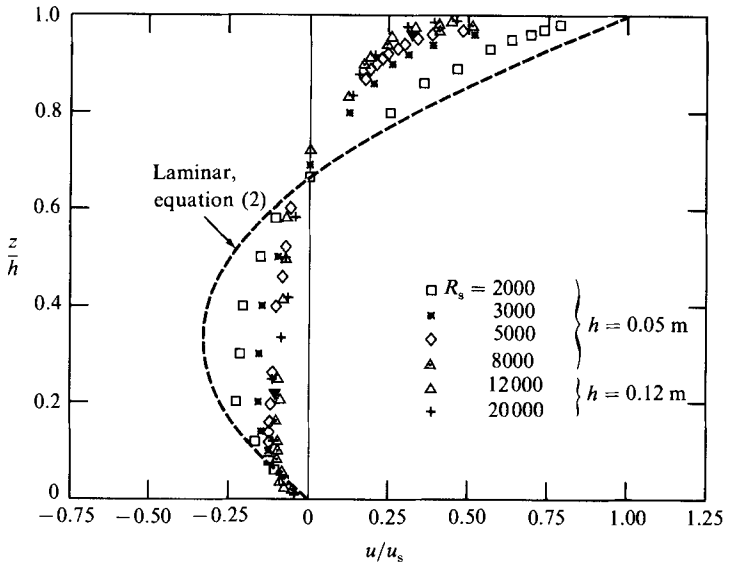

FIGURE 3. Velocity distributions u/u_s *vs.* z/h for six Reynolds numbers and two depths of flow.

countercurrent flow given by the elementary exact solution of the Navier–Stokes equation

$$\frac{u}{u_s} = \frac{z}{h} - 3\frac{z}{h}\left(1 - \frac{z}{h}\right). \tag{2}$$

The juxtaposition of the profile shapes emphasized the fundamental difference that exists between the structures of laminar and turbulent flow. For instance, (2) describes laminar countercurrent flow as a linear superposition of plane Couette flow (first term) and plane Poiseuille flow (second term). That the same is not true for turbulent countercurrent flow is demonstrated in figure 4. The experimental findings presented in this diagram are obtained in three separate plane channel flows of air at roughly comparable turbulent Reynolds numbers, viz. (*a*) plane Poiseuille flow (Leutheusser & Chow 1982) at $R_m = u_m h/v = 21\,500$, where u_m is the maximum velocity in the channel cross-section of aspect ratio $d/h = 10$ ($h = 0.051$ m); (*b*) plane Couette flow (Aydin & Leutheusser 1987) at $R_s = 9200$ and $d/h = 14.4$ ($h = 0.050$ m); and (*c*) countercurrent flow (cf. figure 3) at $R_s = 12000$ and 20000, and $d/h = 6$ ($h = 0.120$ m). Curve (*c**) in figure 4 is the result of a linear superposition of data set (*a*) and data set (*b*) subject to the requirement of zero net flow. The curve differs significantly from the corresponding experimental data over much of the bottom half of the flow and, to a lesser degree, in the vicinity of the shearing surface. The two experimentally determined velocity profiles for $R_s = 12000$ and 20000 are consistent with each other and thereby eliminate Reynolds number as controlling parameter. It follows that any discrepancy, such as the difference between the distinct 'wall-jet'-like hump near the bottom of the cavity in curve (*c**), and its broadened and upwardly shifted counterpart in the experimental data, are likely consequences of a nonlinear interaction between, respectively, a pure pressure-driven flow and a pure shear-driven flow which, in conjunction, constitute the turbulent countercurrent flow under consideration herein.

Synthesis of the velocity field in turbulent countercurrent flow by solving an appropriately 'closed' form of the Reynolds equation of the turbulent mean flow has

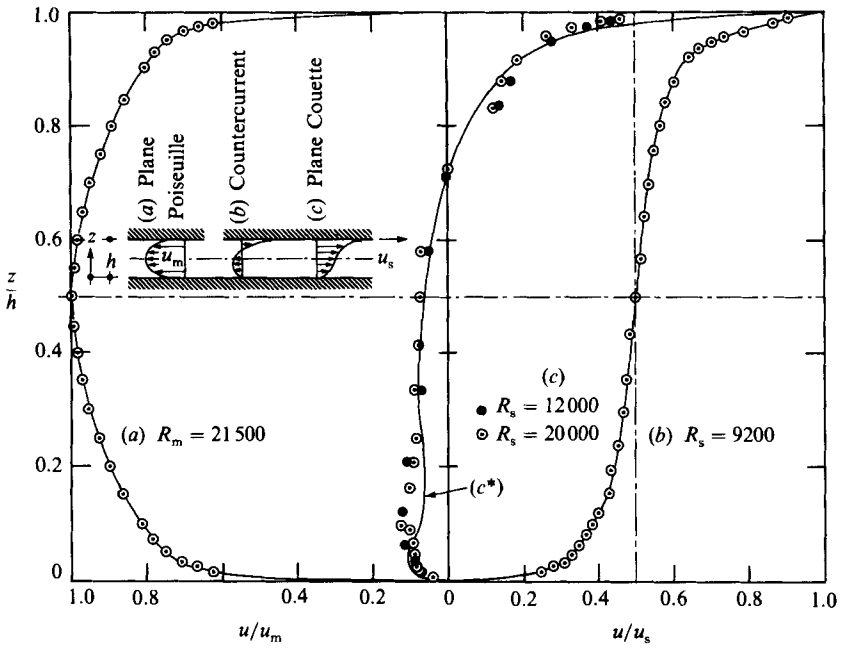

FIGURE 4. Synthesis (curve c^*) of turbulent countercurrent flow by linear superposition of (*a*) plane Poiseuille flow, and (*b*) plane Couette flow. Data set (*c*) is reproduced from figure 3. $R_m = u_m h/\nu$; $R_s = u_s h/\nu$.

frequently been attempted in the past. To this end Reid (1957) assumed a parabolic distribution of the mixing length, Svensson (1978) used a two-equation ($k-\epsilon$) model of turbulence, Koutitas & O'Connor (1980) solved a one-equation ($k-L_0$) model, and Pearce & Cooper (1981) employed a linearly varying eddy viscosity. All of the solutions obtained require prior knowledge of the surface shear stress and the depth of flow, and the numerical predictions differ significantly from each other. Tsanis (1986) has reviewed the matter thoroughly and has proposed an improved method for computing velocity profiles in turbulent countercurrent flow based on the assumption of a parabolic distribution of the eddy viscosity. A typical set of numerical predictions and their experimentally determined counterparts is presented in figure 5. The agreement is quite good and attests to the potential of turbulence modelling for numerically describing complex flows.

The position of zero velocity z_0 in the region of the flow reversal, see figure 1 (*b*), was obtained by averaging data of at least forty instantaneous velocity profiles at the same Reynolds number using video records of smoke-wire images. For each Reynolds number the mean and r.m.s. values of z_0/h were calculated. For Reynolds numbers between 2000 and 20000 these mean values were found to vary between 0.670 and 0.724, while the r.m.s. values ranged from 0.045 to 0.090. A sensitivity analysis was undertaken to examine the error that may be introduced due to the small number of instantaneous velocities. For this purpose, the sample number of instantaneous velocities was varied from 10 to 60, and the resulting means were compared. The maximum error on the position of zero velocity due to the size of samples was found to be 6%. The average position of zero velocity for different Reynolds numbers is presented in figure 6, together with comparable results obtained in conventional air–water systems. This shows that the position of the zero-velocity point stays

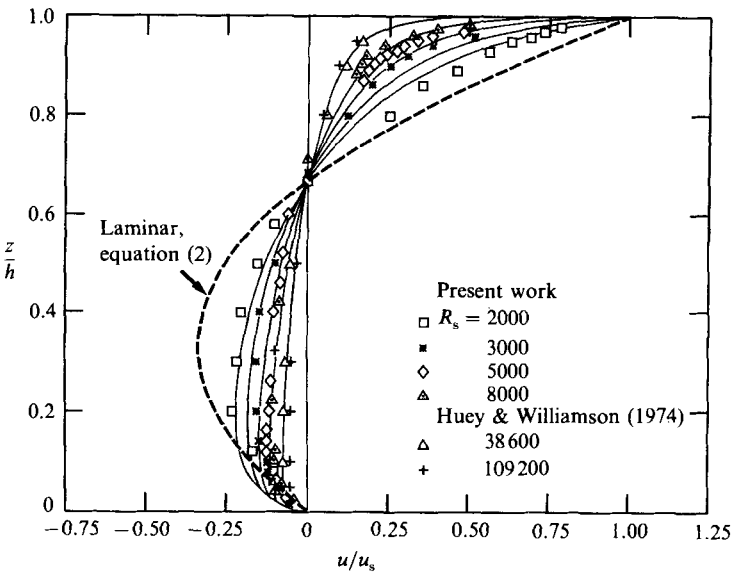

FIGURE 5. Numerically predicted velocity profiles based on a parabolic distribution of the eddy viscosity (Tsanis 1986).

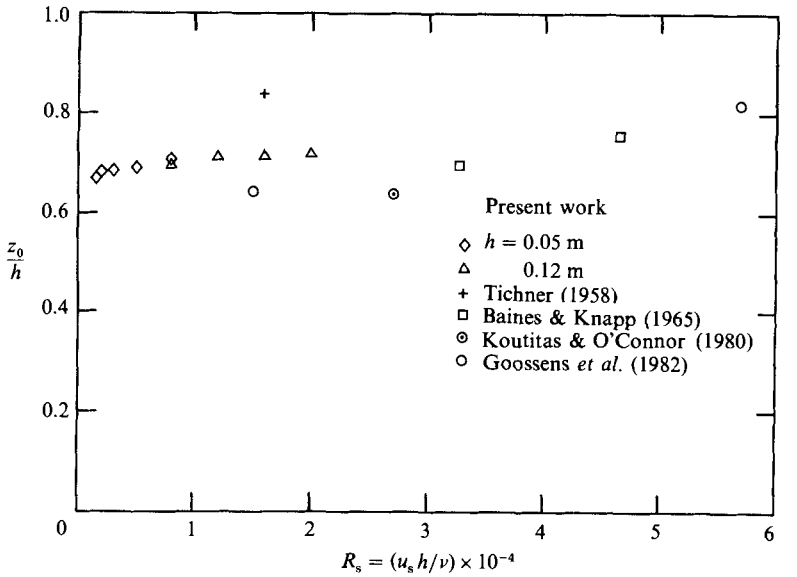

FIGURE 6. Location of zero velocity in the region of flow reversal as a function of Reynolds number.

rather consistently between $z_0/h = 0.60$ and 0.80 for the range of turbulent Reynolds numbers considered. Reference to (2) identifies the zero-velocity position for laminar flows as $z_0/h = 0.67$.

During the tests, velocity measurements were undertaken at points up to 1.5 mm from the shearing surface, and up to 1 mm from the bottom, i.e. well inside the viscous sublayers of the two flow boundaries. This permitted the deduction of the wall shear stress τ and, hence, the shear velocity $u_* = (\tau/\rho)^{\frac{1}{2}}$ from the velocity

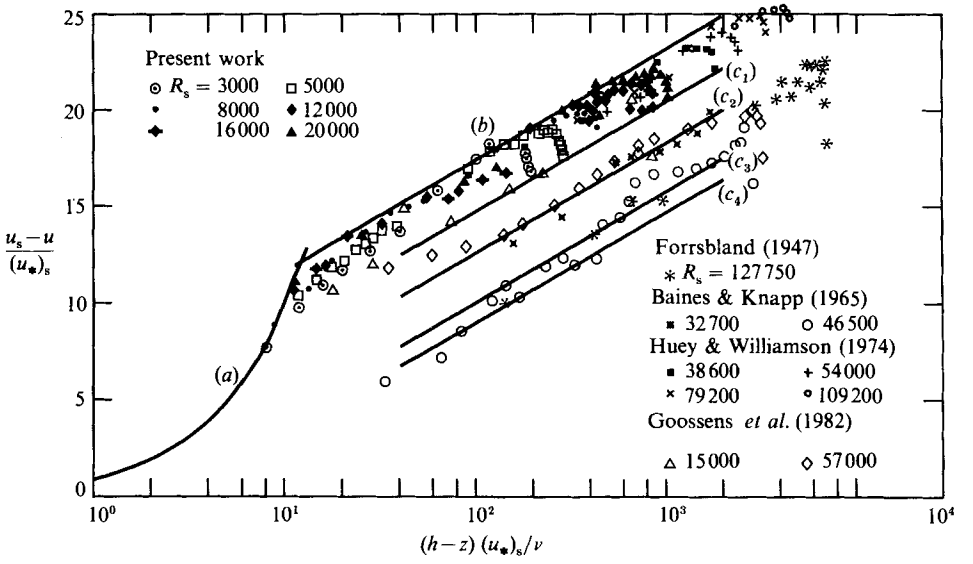

FIGURE 7. Velocity distributions in inner-law coordinates relative to the shearing surface.

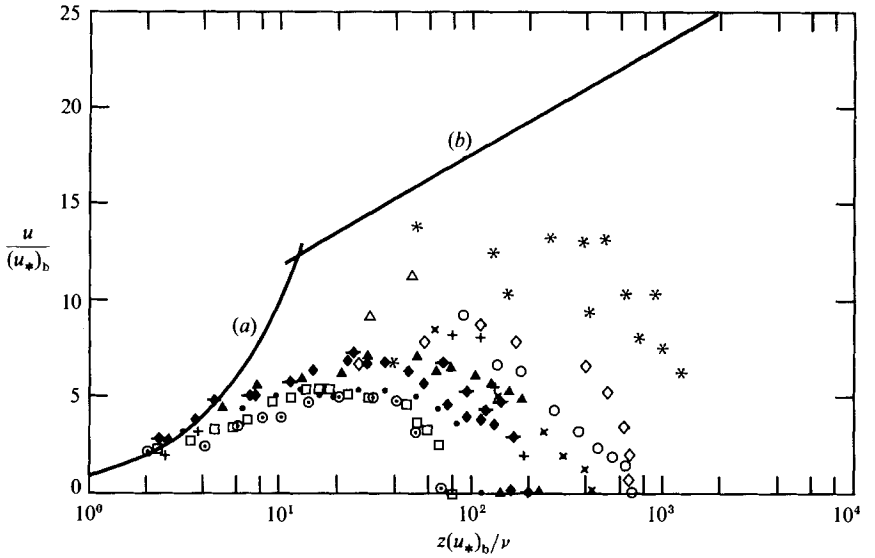

FIGURE 8. Velocity distributions in inner-law coordinates relative to the bottom. Symbols as in figure 7.

gradients at the two walls, and the normalization of the velocity data in terms of the coordinates of the universal, i.e. Reynolds-number independent, 'smooth' inner law of velocity distribution. The present experimental findings, and results of other investigators, are plotted in figures 7 and 8 relative to the shearing surface (subscript s) and bottom (subscript b), respectively.

In figure 7, both the present results and those of Huey & Williamson (1974) obtained in a belt-type apparatus are seen to be in excellent agreement with the firmly established law of the wall for hydrodynamically 'smooth' conditions in fully

developed turbulence. In particular, curve (*a*) represents the viscous sublayer portion of the velocity profile

$$\frac{u_s - u}{(u_*)_s} = \frac{(h-z)(u_*)_s}{\nu}, \tag{3}$$

and curve (*b*), corresponding the logarithmic portion of the velocity profile for hydrodynamically smooth conditions, is described by

$$\frac{u_s - u}{(u_*)_s} = 5.75 \log \frac{(h-z)(u_*)_s}{\nu} + 6.0. \tag{4}$$

On the other hand, findings obtained in combined wind and water tunnels reflect the effects of surface texture due to wave formation. Thus, the curves labelled (C_i) ($i = 1, 2, 3, 4$) are parallel to but below curve (*b*) by the amount of the roughness-induced velocity reduction $\Delta u/(u_*)_s$ which is proportional to the roughness Reynolds number, or von Kármán number $R_k = (u_*)_s k/\nu$, where k is the absolute roughness of the wall.

The velocity reductions are seen to increase with Reynolds number R_s and, clearly, depend also on the laboratory apparatus used. This finding raises questions about the utility of small air–sea interaction tunnels in laboratory studies of wind-induced water currents which, in their natural state, exhibit hydrodynamically smooth shearing surfaces.

A similarly revealing observation is facilitated by figure 8 in which the present and existing velocity data are plotted in inner-law coordinates relative to the bottom; curves (*a*) and (*b*) are plots of the appropriate forms of (3) and (4), respectively. Inspection shows that, in distinct contrast to the conditions prevailing in the shear-driven upper layer, the turbulence in the pressure-driven return portion of the fully spun-up countercurrent flow is quite undeveloped and not tractable by similarity arguments. This structural asymmetry identifies the apparently simple two-dimensional parallel countercurrent flow as an outstanding example of an, in reality, highly complex turbulent shear flow.

3.3. *Law of friction*

The state of universal similarity of the shear-driven upper layer of hydrodynamically smooth countercurrent flow described by (4), and the essential constancy of the position of the point of flow reversal as demonstrated in figure 6 permit the construction of a semi-empirical, quasi-universal relationship for the stress τ_s exerted by the shearing surface on the fluid. In the case of an exposed surface, this shear stress is responsible for the wind-induced tilting of the surface of water bodies known as wind set-up (Leutheusser & Tsanis 1987).

Thus, in terms of a non-dimensional skin-friction coefficient

$$(c_f)_s = \frac{\tau_s}{\frac{1}{2}\rho u_s^2} = 2\left\{\frac{(u_*)_s}{u_s}\right\}^2 \tag{5}$$

and R_s as defined by (1), and by putting $u = 0$ in (4), there follows

$$\left\{\frac{2}{(c_f)_s}\right\}^{\frac{1}{2}} = 5.75 \log\left[R_s\left\{\frac{(c_f)_s}{2}\right\}^{\frac{1}{2}}\right] + 5.75 \log\left\{\frac{h-z_0}{h}\right\} + 6.00. \tag{6}$$

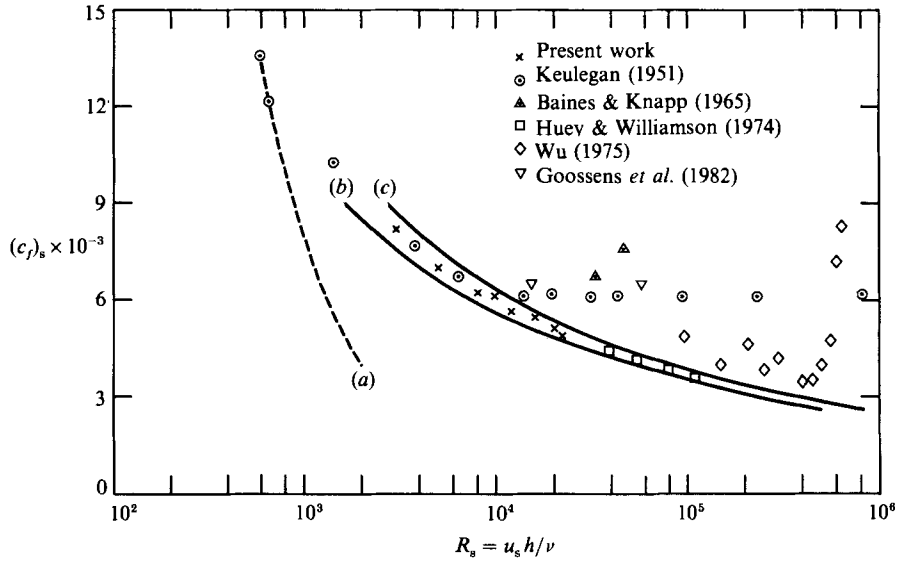

FIGURE 9. Skin-friction coefficient of the shearing surface as a function of Reynolds number. Curve (*a*): equation (7); curves (*b*, *c*): equation (6) with $z_0/h = 0.60$ and 0.80, respectively.

A plot of $(c_f)_s$ *vs.* R_s is presented in figure 9 where curve (*a*) represents the laminar-skin-friction law, readily obtainable from (2),

$$(c_f)_s = \frac{8}{R_s}, \tag{7}$$

and curves (*b*) and (*c*) are plots of (6) for $z_0/h = 0.60$ and 0.80, respectively.

The present experimental data, and those of Huey & Williamson (1974), all obtained under hydrodynamically smooth conditions, are well contained between curves (*b*) and (*c*). This suggests that (6) may be quantified with an average value of $z_0/h = 0.75$, whence it becomes, in standard form,

$$\left\{\frac{1}{(c_f)_s}\right\}^{\frac{1}{2}} = 4.07 \log\{R_s(c_f)_s^{\frac{1}{2}}\} + 1.18. \tag{8}$$

A corresponding universal skin-friction law for hydrodynamically smooth plane Couette flow is (Leutheusser & Chu 1971)

$$\left\{\frac{1}{(c_f)_s}\right\}^{2} = 8.13 \log\{R_s(c_f)_s^{\frac{1}{2}}\} + 6.44; \quad R_s \gtrsim 2 \times 10^4. \tag{9}$$

Comparison of (8) and (9) indicates that the power required to maintain countercurrent flow with zero net flux at, say, $R_s = 10^5$ is about 4.4 times the amount needed by the equivalent plane Couette flow. The power ratio increases slightly with Reynolds number under conditions of turbulent flow. It has the constant value of 4.0 in laminar flow. It follows from this that turbulent countercurrent flow contains more turbulent energy than its Couette equivalent. The relative excess is given by the decimal of the power ratio.

Also included in figure 9 are skin-friction coefficients deduced from experiments in conventional air–water laboratory systems. They form an unordered array above the smooth data and thereby reflect the unpredictable roughness of the interfaces

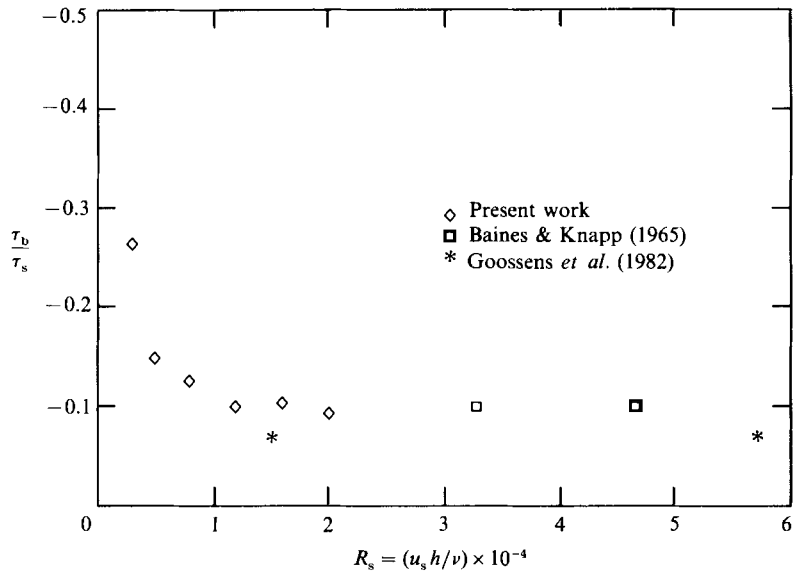

FIGURE 10. Bottom-to-surface shear-stress ratio as a function of Reynolds number.

therein. Keulegan's experiments, in which a surfactant was added to the water in order to suppress surface waves, are in good agreement with (7) for the laminar regime. Under turbulent conditions of flow his data indicate state of hydrodynamic roughness of the free surface with constant relative roughness.

3.4. *Bottom-to-surface shear-stress ratio*

The shear stresses prevailing at the two boundaries of countercurrent flow are proportional to local gradients of the velocity profile. Their ratio, τ_b/τ_s, as determined in the present experiments, and corresponding results obtained in conventional air–water systems are plotted as a function of Reynolds number in figure 10. The bottom-to-surface shear-stress ratio has the constant value -0.50 in laminar flow. Under turbulent conditions, and seemingly irrespective of the hydrodynamic state of the interface, the magnitude of this ratio decreases with increasing Reynolds number. It reaches a value of approximately -0.10 in the present case, and this is in good agreement with findings obtained in conventional air–water systems.

3.5. *Longitudinal pressure gradient*

The requirement of zero net mass flux characterizing countercurrent flow necessitates a pressure gradient $\mathrm{d}P/\mathrm{d}x$ to drive the return current. This gradient is readily obtained from a force balance whence, with (1) and (5), there follows, in convenient non-dimensional form,

$$\frac{h^2}{\mu u_s}\frac{\mathrm{d}P}{\mathrm{d}x} = (c_f)_s R_s \frac{1}{2}\left(1-\frac{\tau_b}{\tau_s}\right), \tag{10}$$

which is valid for all conditions of flow.

In laminar flow the right-hand side of (10) has the constant value 6.00. A plot of (10) for turbulent flow, with $(c_f)_s$ given by (8) and $\tau_b/\tau_s = -0.10$, is represented by the solid, and essentially straight line in figure 11. Also shown are discrete results of the present investigation, and corresponding data obtained by Huey & Williamson

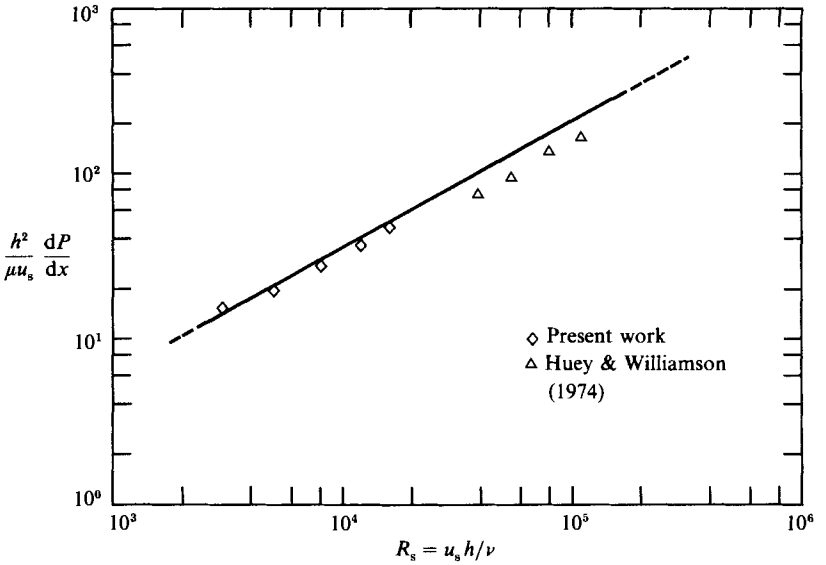

FIGURE 11. Non-dimensional longitudinal pressure as a function of Reynolds number.

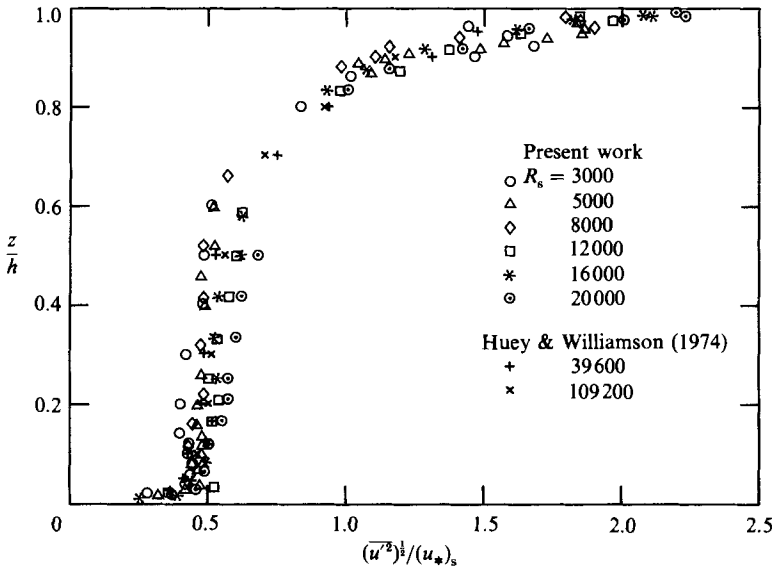

FIGURE 12. Streamwise intensities of turbulence as a function of transverse position.

(1974). All findings are consistent with each other and indicate that, under hydrodynamically smooth conditions, the non-dimensional pressure gradient increases with Reynolds number in accordance with the approximate relation

$$\frac{h^2}{\mu u_s}\frac{dP}{dx} = 0.0274 R_s^{0.7765}. \tag{11}$$

No similarly definite deduction is possible for the pressure gradient occurring in conventional air–water systems because of the uncertain state of the interfaces therein.

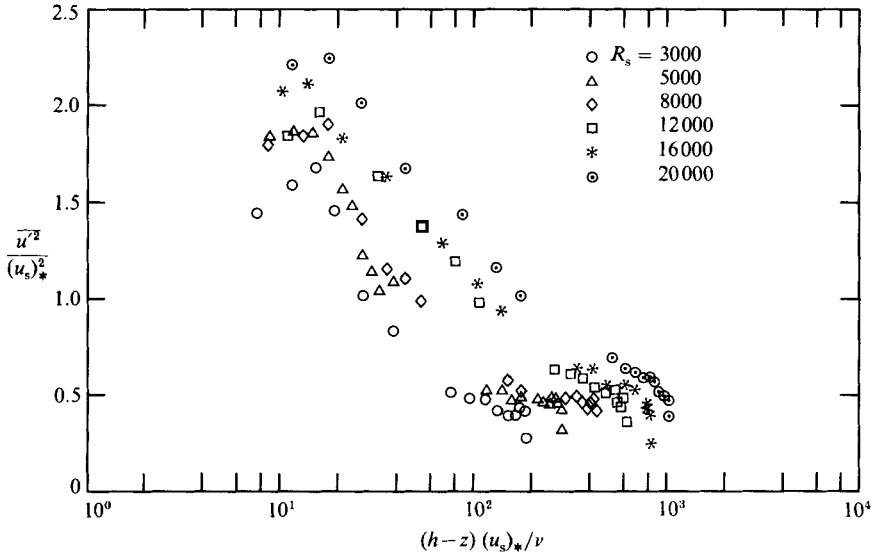

FIGURE 13. Distributions of the streamwise intensity of turbulence in inner-law coordinates relative to the shearing surface.

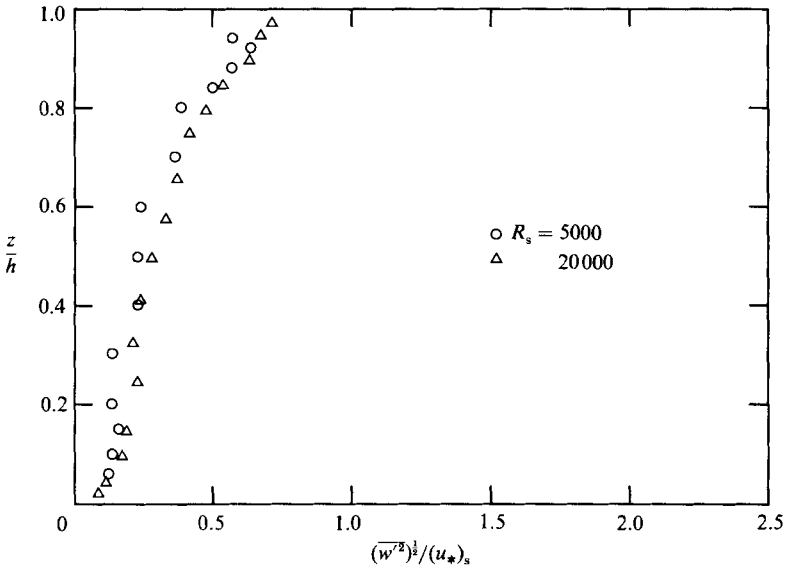

FIGURE 14. Transverse intensities of turbulence as a function of transverse position.

3.6. *Turbulence intensities and Reynolds stresses*

Turbulence intensities in the streamwise direction, normalized by the surface shear velocity, are presented in figure 12 as a function of position z/h, for six Reynolds numbers between 3000 and 20000. Also included are comparable results reported by Huey & Williamson (1974). The non-dimensional intensities are nearly constant in the region of return flow, but then increase rapidly to a value of 2.35 near the shearing surface, which agrees with the findings of Baines & Knapp (1965). In figure 13, the present measurements of streamwise turbulence intensity are plotted in terms of inner-law coordinates relative to the shearing surface. As is usual with turbulence

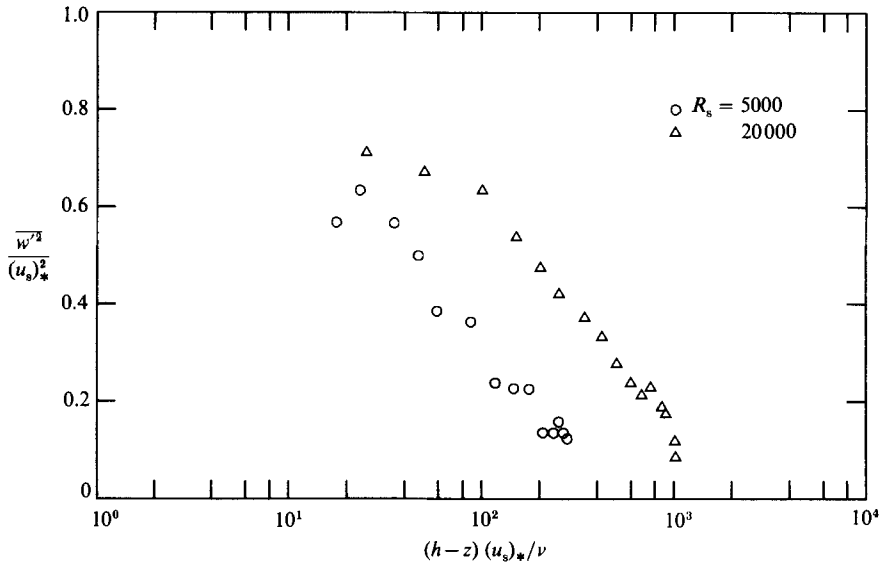

FIGURE 15. Distributions of the transverse intensity of turbulence in inner-law coordinates relative to the shearing surface.

quantities, and in distinct contrast to mean velocities, the normalized intensities behave only in a quasi-universal fashion, and increase somewhat with Reynolds number. Nevertheless, all intensity profiles have a maximum at $(h-z)(u_*)_s/\nu \approx 18$. Corresponding findings for the turbulence intensities in the transverse, or z-direction are presented in figures 14 and 15.

Reynolds stresses, like the transverse turbulence intensities depicted in figures 14 and 15, were obtained at two Reynolds numbers, viz. $R_s = 5000$ at $h = 0.05$ m, and $R_s = 20000$ at $h = 0.12$ m, respectively. The present results for the turbulent shear stresses, together with existing experimental data, and the theoretically linear shear-stress distributions for laminar and high-Reynolds-number turbulent flow ($\tau_b/\tau_s = -0.10$) are presented in figure 16. The Reynolds stresses from the present work are also plotted in terms of inner-law coordinates relative to the shearing surface in figure 17.

It can be seen in figure 16 that all of the available experimentally deduced Reynolds stresses differ significantly from a linear distribution. The stresses decrease with increasing distance from the shearing surface and assume essentially constant values in the core of the flow. The present data are consistent with findings obtained in conventional air–water systems. However, comparison between the distributions for $R_s = 5000$ and $R_s = 20000$ shows that the Reynolds stresses for $h = 0.05$ m are much closer to the theoretical distribution than those obtained for $h = 0.12$ m. The same trend is exhibited by the experimental data of Goossens *et al.* (1982) and may be an indication of one or both of non-negligible effects due to the necessarily finite magnitude of the longitudinal aspect ratio $1/d$ of the laboratory flow field (20 and 48 in the present instance), and an immature state of the structure of turbulence at the relatively low Reynolds numbers used in the experiments.

The latter conjecture has some support in the undeveloped inner-law plot of the axial mean velocity in the bottom portion of the flow depicted in figure 8. However, no ready explanation can be offered to reconcile the findings displayed in figure 16 with the excellent agreement between theory and experiment reported by El

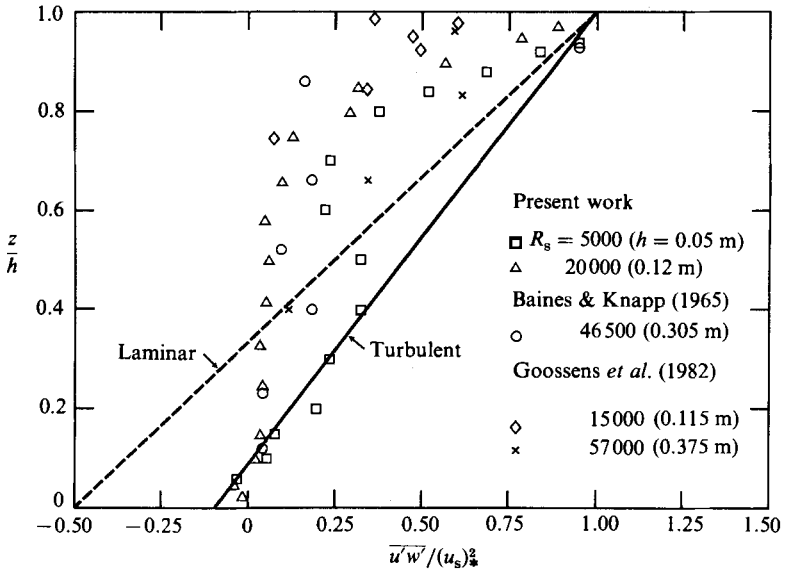

FIGURE 16. Reynolds stresses as a function of transverse position.

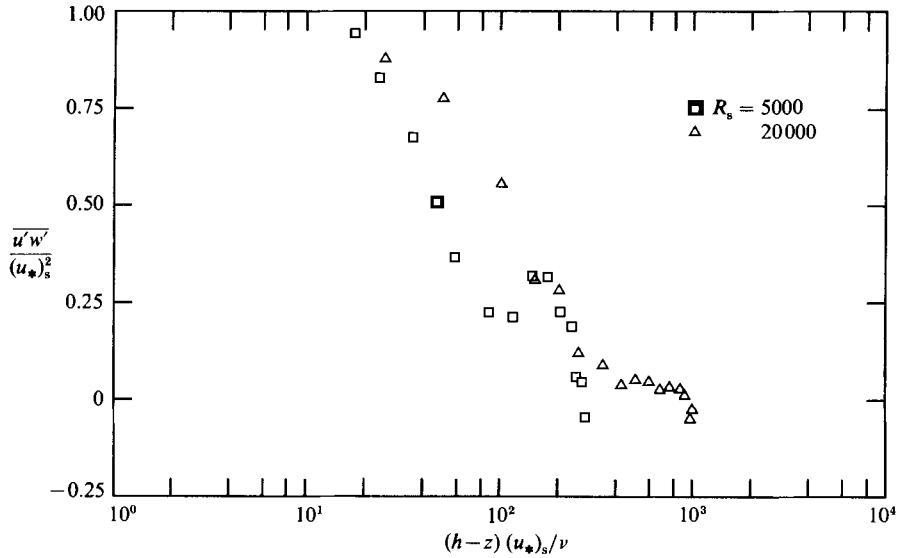

FIGURE 17. Distributions of Reynolds stress in inner-law coordinates relative to the shearing surface.

Telbany & Reynolds (1981) for their shear-stress measurements in both pressure- and shear-driven plane channel flows. While none of their experiments correspond precisely to the countercurrent flow with zero net flux under consideration herein, the tests cover the same ranges of Reynolds number and longitudinal aspect ratio as those included in figure 16. The fact that El Telbany & Reynolds (1981) find perfectly linear shear-stress distributions, while the various investigators referred to in figure 16 are unable to do so under comparable circumstances, is further evidence of the complexity of these supposedly simple flows.

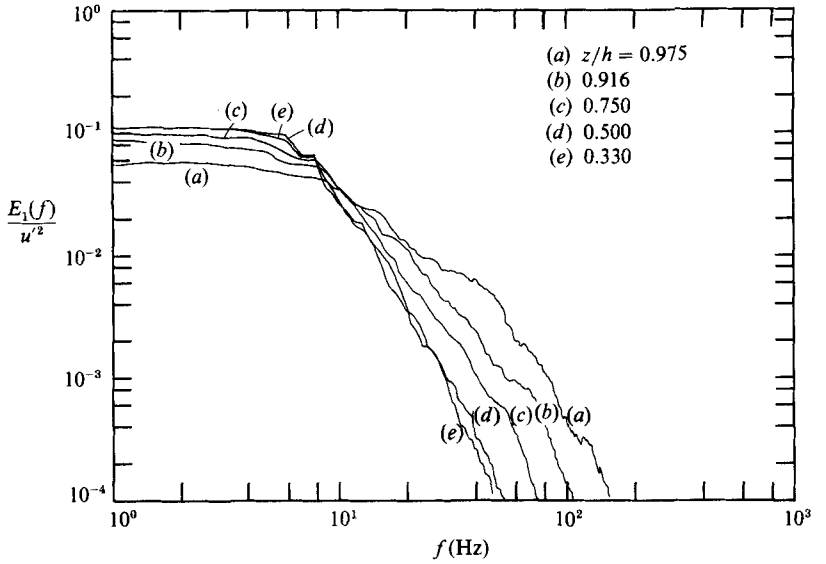

FIGURE 18. Autospectra of the streamwise turbulence component for five transverse positions; $R_s = 20000$.

3.7. *Turbulence spectra and macroscale*

The autospectrum of turbulence represents the distribution of streamwise energy $E_1(f)$ normalized with the variance $\overline{u'^2}$ as a function of frequency f. In the present work, spectra were determined at various wall distances and Reynolds numbers in a flow with $h = 0.12$ m. As an example, in figure 18 are presented spectra for five wall distances at Reynolds number $R_s = 20000$. The curves indicate an enhanced involvement of the lower frequencies with increasing distance from the shearing surface. The distribution of the spectral energy is essentially the same throughout the return portion of the flow, thereby reflecting the constancy of turbulence intensity in this region.

An illustration of the influence of Reynolds number on the local distribution of spectral energy is presented in figure 19. This demonstrates a growing participation of higher frequency components with increasing Reynolds number. The energy spectra of figure 19 are expressed relative to the macroscale, or integral scale of turbulence, T_m, and are shown together with the theoretical spectrum for isotropic turbulence behind a grid, curve (*A*) (Dryden 1943), and Huey & Williamson's (1974) experimental results. The latter's data, obtained at $z/h = 0.850$ for Reynolds numbers from 38600 to 109200, collapse into a single curve and are in generally good agreement with the theoretical spectrum. On the other hand, the present findings, at $z/h = 0.975$, for Reynolds numbers from 8000 to 12000 only tend asymptotically toward these results. However, for Reynolds numbers over 16000, the present spectral distributions follow the same pattern as those of Huey & Williamson (1974) and, thus, give further evidence of a state of fully developed turbulence near the shearing surface at high Reynolds numbers.

The variation of the macroscale of turbulence with Reynolds number corresponding to figure 19 is displayed in figure 20. The macroscale is rendered non-dimensional in terms of u_s and h order to facilitate comparison of findings from various sources. The two sets of data included in the figure are consistent with each

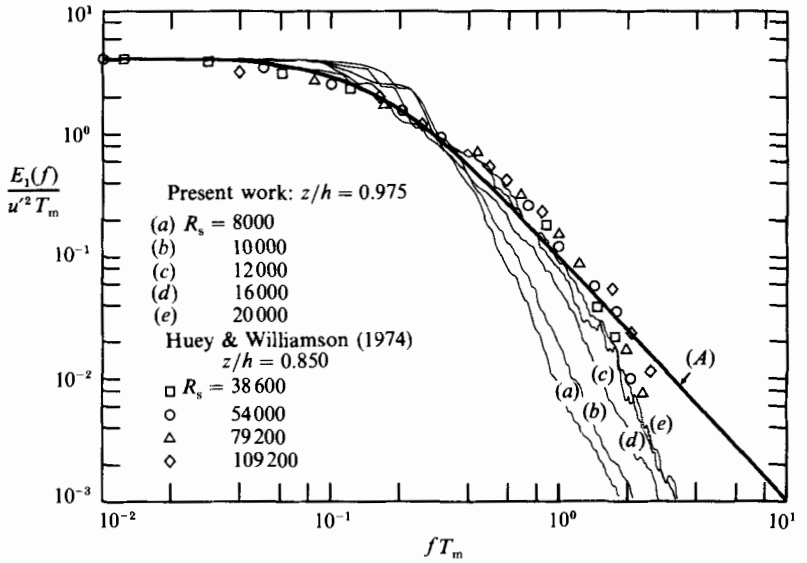

FIGURE 19. Local energy spectra of the macroscale, for various Reynolds numbers; curve (*A*) is Dryden's (1943) theoretical spectrum for isotropic turbulence.

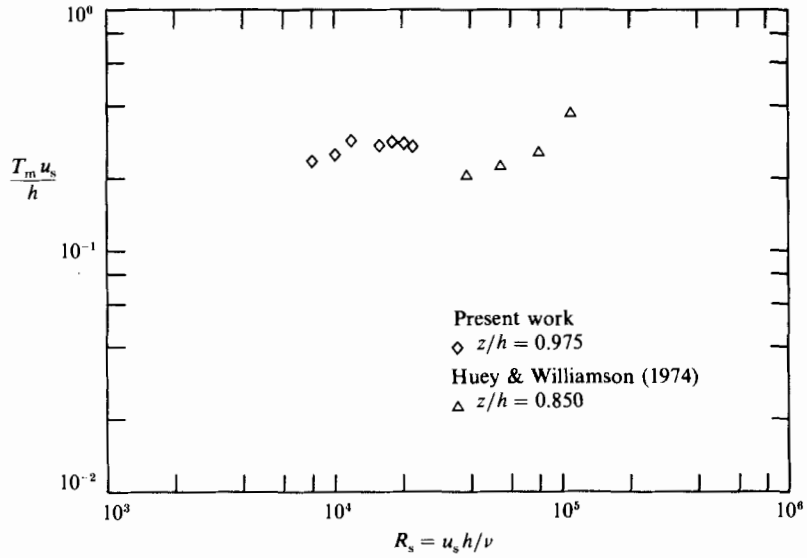

FIGURE 20. Non-dimensional macroscale of turbulence, corresponding to the data of figure 19, as a function of Reynolds number.

other, with values of the non-dimensional macroscale ranging between 0.16 and 0.30 irrespective of Reynolds number.

4. Conclusions

The shear-induced countercurrent flow with zero net mass flux studied in this paper is a member of the general family of plane channel flows which encompasses all possible combinations from purely pressure-driven to purely shear-driven basic

flows. Under laminar conditions, these fluid motions are described by simple exact solutions of the Navier–Stokes equation and constitute linear superpositions of the basic flows.

It is shown in this paper that, once turbulence prevails, the point of transition depending on the particular combination of basic flows involved, the principle of superposition fails in detail. The nonlinear interaction between the basic flows intimated by this finding, and the finite length of the driven cavity may be partially responsible for some of the aberrations observed in the course of the present and related works. These include the apparent impossibility of experimentally verifying linear shear-stress distributions, and the evidence of structural asymmetry between the shear-induced drift current and the pressure-driven return current of the flow under consideration.

Apart from these peculiarities, however, the paper provides well-substantiated findings on turbulence characteristics and engineering quantities for hydrodynamically smooth wall conditions which greatly enhance the present understanding of this technically important fluid motion. The behaviour of transitional and fully turbulent countercurrent flow is reflected in the spectrum of turbulence energy normalized by the macroscale. Correlations of velocity data, and the results of spectral analysis under fully developed turbulent conditions identify the studied countercurrent flow as consistent with other turbulent wall-shear flows in spite of its small mean velocities and large turbulence intensities. A quasi-universal skin-friction law is proposed which should prove useful in the modelling of wind-driven water currents, and thin fluid films in high-speed bearings. The law suggests that countercurrent flow has a higher content of turbulent energy and, hence, a greater mixing potential than the equivalent Couette flow. Finally, it may be noted that the experimental results presented in this paper, and their support by data of other researchers, confirm the 'driven-cavity'-type laboratory system used in the investigation as a viable research tool for detailed studies of countercurrent flow.

The work reported herein was supported through Grant A-1541 of the Natural Sciences and Engineering Research Council of Canada.

REFERENCES

AYDIN, M. & LEUTHEUSSER, H. J. 1979 Novel experimental facility for the study of plane Couette flow. *Rev. Sci. Instrum.* **50**, 1362–1366.

AYDIN, M. & LEUTHEUSSER, H. J. 1980 Very low velocity calibration and application of hot-wire probes. *DISA Information*, No. 25, pp. 17–18.

AYDIN, E. M. & LEUTHEUSSER, H. J. 1987 Experimental investigation of turbulent plane-Couette flow. *ASME Applied Mechanics, Bioengineering, and Fluids Engineering Conf., Cincinnati, OH, June 14–17, 1987, Forum on Turbulent Flows,* FED-Vol. 51, pp. 51–54.

BAINES, W. D. & KNAPP, D. J. 1965 Wind-driven water currents. *J. Hydraul. Div. ASCE* **91** (HY2), 205–221.

BENDAT, J. S. & PIERSOL, A. G. 1971 *Random Data: Analysis and Measurement Procedures.* Wiley.

DRYDEN, H. L. 1943 A review of the statistical theory of turbulence. *Q. Appl. Maths* **1**, 7–42.

EL TELBANY, M. M. M. & REYNOLDS, A. J. 1981 Turbulence in plane channel flows. *J. Fluid Mech.* **111**, 283–318.

FORRSBLAND, L. 1947 Effects of wind, waves, and currents in floating timber. *Bulletin No. 7, Institute of Hydraulics.* Royal Institute of Technology, Stockholm, Sweden.

GATSKI, T. B., GROSH, C. E. & ROSE, M. E. 1982 A numerical study of the two-dimensional Navier-Stokes equation in vorticity–velocity variables. *J. Comp. Phys.* **48**, 1–22.

GOLDSTEIN, R. J. (ed.) 1983 *Fluid Mechanics Measurements.* Hemisphere.

GOOSSENS, L. 1979 Reservoir destratification with bubble columns. Doctoral thesis, Delft University of Technology, Delft, The Netherlands.

GOOSSENS, L. T., VAN PAGEE, H. J. A. & TESSEL, P. J. 1982 Vertical diffusion in air-driven water flows. *J. Hydraul. Div. ASCE* **108** (HY2), 995–1009.

GUSTAFSON, K. & HALASI, K. 1986 Vortex dynamics of cavity flows. *J. Comp. Phys.* **64**, 279–319.

HUEY, L. J. & WILLIAMSON, J. W. 1974 Plane turbulent Couette flow with zero net-flow. *Trans. ASME* E: *J. Appl. Mech.*, pp. 885–890.

KEULEGAN, G. H. 1951 Wind tides in small closed channels. *Journal of Research, Natl Bur. Stand. J. Res.* **46**, 358–381.

KOUTITAS, C. & O'CONNOR, B. 1980 Modeling three-dimensional wind-induced flows. *J. Hydraul. Div. ASCE* **106** (HY11), 1843–1865.

LEUTHEUSSER, H. J. & CHOW, R. S. 1982 Characteristics of the turbulent mean flow in a two-dimensional channel. In *Proc. Intl Symp. on Urban Hydrology, Hydraulics and Sediment Control, University of Kentucky, Lexington, KY, July 27–29, 1982*, pp. 431–436.

LEUTHEUSSER, H. J. & CHU, V. H. 1971 Experiments on plane Couette flow. *J. Hydraul. Div. ASCE* **97** (HY9), 1269–1284.

LEUTHEUSSER, H. J. & TSANIS, I. K. 1987 Dependence of wind set-up on Reynolds number of induced flow. In *Proc. 22nd Congress of The International Association for Hydraulic Research, Lausanne, Switzerland, August 31–September 4, 1987, Topics in Lake and Reservoir Hydraulics,* Vol. C1, pp. 132–136.

LUMLEY, J. L. & PANOFSKY, H. A. 1964 *The Structure of Atmospheric Turbulence.* Interscience (Wiley).

MASCH, F. D. 1963 Mixing and dispersion of wastes by wind and wave action. *Intl J. Air Wat. Pollut.* **7**, 697–720.

PEARCE, B. P. & COOPER, C. K. 1981 Numerical circulation model for wind-induced flow. *J. Hydraul. Div. ASCE* **107** (HY3), 285–302.

REICHARDT, H. 1956 Üeber die Geschwindigkeitsvertteilung in einer gradlinigen turbulenten Couettesteoemung, *Z. Angew. Math. Mech.* S26–S29.

REID, R. O. 1957 Modification of the quadratic bottom-stress law of turbulent channel flow in the presence of surface wind-stress. *Tech. Mem.* 93, Beach Erosion Board, US Department of the Army, Washington, D.C.

SVENSSON, U. 1978 Mathematical model of the seasonal thermodine. *Rep.* 1002, Department of Water Resources Engineering, University of Lund, Lund, Sweden.

TICHNER, E. G. 1958 Transient wind tides in shallow water. *Series 71, Issue 11,* Institute of Engineering Research, Berkeley, California.

TSANIS, I. K. 1986 Characteristics of shear-induced countercurrent flow. Doctoral thesis, University of Toronto, Toronto, Ontario, Canada.

TSANIS, I. K. 1987 Calibration of hot-wire anemometers at very low velocities. *Dantec Information,* No. 4, February, pp. 13–14.

TSANIS, I. K. & LEUTHEUSSER, H. J. 1987 An example of transient laminar counter-current flow. *Trans. ASME* I: *J. Fluids Engng* **109**, 262–267.

VAGT, J. D. 1979 Hot-wire probes in low speed flow. *Prog. Aero. Sci.* **18**, 271–323.

WU, J. 1973 Prediction of near-surface drift currents from wind velocity. *J. Hydraul. Div. ASCE* **99** (HY9), 1291–1302.

WU, J. 1975 Wind-induced drift currents. *J. Fluid Mech.* **68**, 49–70.